

A complete view of the outskirts of the Coma cluster

M. S. Mirakhor^{1*} and S. A. Walker¹

¹Department of Physics and Astronomy, University of Alabama in Huntsville, Huntsville, AL 35899, USA

ABSTRACT

We present a new extended *XMM-Newton* mosaic of the nearby Coma cluster, which covers the cluster out to the virial radius with nearly complete azimuthal coverage. This large mosaic is combined with the *Planck* Sunyaev Zel’dovich effect observations to recover the thermodynamic properties of the intracluster medium in an azimuthally averaged profile and 36 angular sectors, producing the highest spatial resolution view of the thermodynamics of the outskirts of a galaxy cluster in its entirety. Beyond r_{500} , our clumping corrected entropy measurements along the less disturbed directions are statistically consistent with the power-law entropy profile predicted by non-radiative simulations, and the gas mass fraction agrees with the mean cosmic baryon fraction. However, there is a clear entropy deficit in the outskirts to the southwest, coinciding with where Coma connects to a cosmic web filament which joins it to Abell 1367. The low entropy to the southwest extends from $0.5-1.0r_{200}$, and is consistent with what is expected from simulations of a filamentary gas stream penetrating into the cluster as it continues to accrete matter from the cosmic web. We also find that the radial profiles of the recovered quantities become increasingly asymmetric in the outskirts, particularly along the more disturbed directions, consistent with the predictions of cosmological simulations.

Key words: galaxies: clusters: intracluster medium - intergalactic medium - X-rays: galaxies: clusters

1 INTRODUCTION

Accurate measurements of the intracluster medium (ICM) of galaxy clusters to the virial radius are important for many reasons. The virial radius represents the boundary within which the cluster ICM is expected to be virialised, and outside of which matter is still accreting onto the cluster as it continues to form. Studying cluster outskirts allows the cluster formation process to be understood, thus constraining simulations of cluster formation and models for the baryon fractions of clusters. We can also investigate where the assumption of hydrostatic equilibrium breaks down, which is important for calculating the masses of galaxy clusters, and using clusters as cosmological probes. For a review see Walker et al. (2019).

Due to the very low X-ray surface brightness in cluster outskirts, accurate measurements of the ICM around the virial radius are highly challenging. Systematic uncertainties in the modelling of the *XMM-Newton* background mean that finding gas temperatures through spectral fitting outside r_{500} (which is around 65 percent of the virial radius, r_{200}) is generally impossible with *XMM-Newton*. One new approach, which gets around these limitations, is to combine X-ray surface brightness measurements with *Planck* Sunyaev Zeldovich effect (SZ) measurements (Tchernin et al. 2016; Eckert et al. 2017; Ghirardini et al. 2018; Ghirardini et al. 2019). For plasma with temperatures above 1.5 keV, the X-ray surface brightness in the soft band 0.7-1.2 keV can be trivially converted into

gas density, as it has very little dependence on the gas temperature. These gas densities, n_e , can then be combined with the pressure measurements, P , from *Planck* to obtain the gas temperature, $kT = P/n_e$, and the gas entropy, $K = kT/n_e^{2/3} = P/n_e^{5/3}$.

Simulations of galaxy cluster formation (e.g. Roncarelli et al. 2006, Vazza et al. 2011, Avestruz et al. 2014, Lau et al. 2015) predict that clusters become increasingly asymmetric in both density and temperature in the outskirts, where the cluster joins onto the surrounding cosmic web. Such simulations predict azimuthal variations in the region between r_{500} and r_{200} due to the asymmetric nature of accretion onto galaxies clusters from the cosmic web, and these can only be resolved by dividing the cluster into small enough sectors. Simulations (e.g. Gaspari & Churazov 2013) indicate that the peak of the power spectrum of gas motions in galaxy clusters should lie in the range 250-500kpc, so it is important to be able to study the ICM properties on these scales. The simulations of Zinger et al. (2016, 2018) have found that the gas streams from the filaments of the cosmic web can penetrate deep into unrelaxed clusters, transporting low entropy gas and large amounts of momentum and energy into their central regions.

At present, unravelling and mapping this fine structure in the outskirts of clusters has proven difficult for a number of reasons. As a result, our measurements of cluster outskirts are typically limited to azimuthally averaged profiles, which are clearly not telling us the full story of what is happening in the outskirts.

Direct X-ray observations of gas temperatures with *Suzaku*, which had a much lower and more stable background than *XMM-*

* Email: msm0033@uah.edu

Newton (*Suzaku*'s particle background was a quarter of that of *XMM-Newton*'s due to *Suzaku*'s low Earth orbit) were limited in their spatial resolution due to *Suzaku*'s large point spread function (PSF) of 2 arcmin, and limited in their azimuthal coverage by *Suzaku*'s small field of view of $17.8 \text{ arcmin} \times 17.8 \text{ arcmin}$ (see Walker et al. 2019 for a review). Observing strategies with *Suzaku* could be divided into two groups. The first focused on high azimuthal coverage of higher redshift clusters with low spatial resolution (e.g. Kawaharada et al. 2010, Walker et al. 2012a, Walker et al. 2012b, Sato et al. 2012, Ichikawa et al. 2013). The second focused on getting around *Suzaku*'s large PSF by looking at nearby clusters to achieve high spatial resolution (Simionescu et al. 2011, Urban et al. 2014), Centaurus (Walker et al. 2013), Coma (Simionescu et al. 2013) and Virgo (Simionescu et al. 2017). However the small field of view of *Suzaku* meant that the coverage of these nearby clusters was limited to strips covering at most 30 percent of the virial radius.

The method of combining XMM surface brightness with *Planck* pressure measurements is also limited by the large PSF of *Planck* ($\sim 10 \text{ arcmin}$ FWHM). To make progress in understanding the detailed physics in the outskirts of clusters, we therefore need to study low redshift clusters, whose large angular extents allow us to circumvent the large PSF of *Planck*. Thanks to XMM's larger field of view an approximately circular field with a diameter of 30 arcmin, and the fact that we only require surface brightness measurements to combine with the existing *Planck* pressures rather than detailed X-ray spectroscopy, mapping campaigns of nearby clusters with full coverage out to their virial radii can provide us with the best ever view of the outskirts of galaxy clusters.

As described by the Planck collaboration itself, the Coma cluster is 'the most spectacular SZ source in the Planck sky' (Planck Collaboration X 2013). As one of the nearest massive clusters in the universe ($M_{500} \approx 6.0 \times 10^{14} M_{\odot}$ at redshift 0.023), *Planck* was able to detect the SZ emission in Coma with extremely high signal to noise (> 22) over a 5×5 degree area. *Planck* was able to measure the SZ signal in Coma out to colossal radii, out to 2 times the virial radius ($2r_{200}$).

At the low redshift of Coma, the *Planck* beam size of 10 arcmin (FWHM) corresponds to a physical size of 280 kpc, which is sufficient resolution to test the predictions of numerical simulations for the asymmetric distribution of temperature and entropy in cluster outskirts. Malavasi et al. (2020) have used Sloan Digital Sky Survey (SDSS) to show that the Coma cluster is a highly connected structure, with three main connections to cosmic web filaments to the northeast, north and south west. This makes Coma an excellent target to study the azimuthal variation of the ICM's thermodynamic properties, and how these relate to Coma's larger scale environment.

Here we present our new extended *XMM-Newton* mosaic of the Coma cluster, which covers the cluster out to r_{200} with nearly complete azimuthal coverage (the XMM mosaic covers 90 percent of the cluster inside r_{200}). By combining the X-ray surface brightness information from this mosaic with the *Planck* SZ data for Coma, we are able to produce the highest spatial resolution view of the thermodynamics of the outskirts of a galaxy cluster ever achieved.

Planck Collaboration X (2013) estimated the $Y_X = M_{\text{gas}} \times kT$ parameter of the Coma cluster iteratively using the $Y_X - M_{500}$ scaling relation calibrated from hydrostatic mass estimates in a nearby cluster system (Arnaud et al. 2010), and found that the scale radius of Coma at a density 500 times the critical density of the universe to be $r_{500} = 47 \text{ arcmin}$. We adopt this value throughout the

paper, and this implies the scale radius $r_{200} \approx 70 \text{ arcmin}$, using the relation $r_{500} = 0.65r_{200}$ obtained assuming an NFW profile with a concentration parameter of 4. These are the same values used in the study of the *Suzaku* observations in Simionescu et al. (2013).

The paper is structured as follows: in Section 2 we describe the X-ray and SZ effect data used in this work; the analysis procedures for our data are presented in Section 3; in Section 4 we show the reconstructed profiles of the thermodynamic properties of the ICM; we present the analysis in angular sectors in Section 5; our findings are discussed in Section 6; and our conclusions are presented in Section 7. Throughout this paper, we adopt a Λ CDM cosmology with $\Omega_m = 0.3$, $\Omega_{\Lambda} = 0.7$, and $H_0 = 100 h_{100} \text{ km s}^{-1} \text{ Mpc}^{-1}$ with $h_{100} = 0.7$. At the redshift of Coma, 1 arcmin corresponds to 28 kpc.

2 DATA

2.1 XMM-Newton

A large mosaic of *XMM-Newton* observations was obtained during the AO-18 cycle (PI: S. A. Walker). The new mosaic consists of 11 pointings, with 9 of which covering the outskirts region of the cluster between r_{500} and r_{200} , whereas 2 pointings covering the local sky background of the cluster in two different positions. The exposure time ranges between 23 and 35 ks each, for a total exposure time of 300 ks. We combined these observations with the 50 existing *XMM-Newton* observations in the field of the Coma cluster that cover, mainly, the central and intermediate regions of the cluster. These archive observations were performed in the period between 2000 and 2019, and their total observing time is around 2.0 Ms. The details regarding all 61 of the *XMM-Newton* observations used in this work are summarized in Table A1.

2.2 Planck

The Coma Cluster was also observed by the *Planck* satellite in nine frequency bands covering 30–857 GHz. The SZ effect signal detected towards Coma is significant with a signal to noise ratio > 22 (Planck Collaboration VIII 2011). *Planck* was able to measure the SZ effect signal in Coma out to large radii, out to at least two times the virial radius. The data used in this paper based on the *Planck* nominal survey that carried out between 2009 August 13 and 2010 November 27.

3 ANALYSIS PROCEDURES

3.1 XMM-Newton analysis

The X-ray data for all 61 observations in this work were reduced using the *XMM-Newton* Science Analysis System, XMM-SAS v18.0, and the calibration files, following the procedures illustrated in the Extended Source Analysis Software manual (ESAS, Snowden & Kuntz 2014). We initially processed the data using the *epchain* and *emchain* scripts, and then used ESAS tasks *mos-filter* and *pn-filter* to remove soft proton flares and create clean event files. The data were then examined for CCDs in anomalous states, and any affected CCDs were excluded from the analysis. Point sources and extended substructures that contaminated the field of view were masked and removed by running the ESAS tool *cheese*. For all *XMM-Newton* detectors, the required intermediate spectra and response files for the entire region of interest were created using the

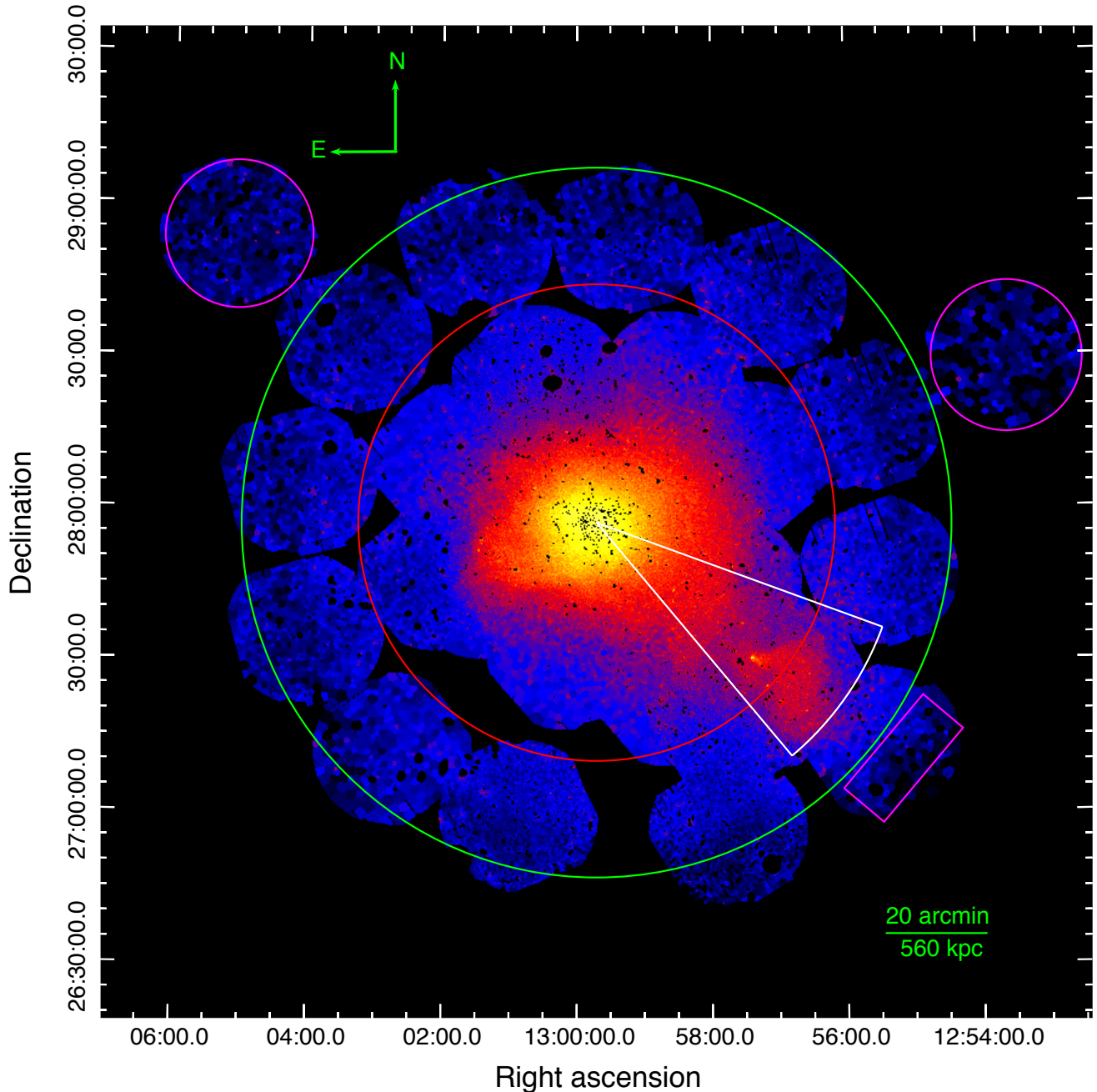


Figure 1. *XMM-Newton* mosaicked and Voronoi tessellated image of the Coma cluster in the 0.71.2 keV energy band. North is up and east is to the left. The red and green circles show, respectively, the locations of r_{500} and r_{200} . The magenta regions show the regions in which the local background counts were extracted, and the white sector indicates the region which is excluded from the analysis as it contains the infalling group NGC 4839.

mos-spectra and *pn-spectra* tasks. These files were then used to create the quiescent particle background (QPB) spectra and images by running the ESAS procedures *mos-back* and *pn-back*.

We also filtered the data for any residual soft proton contamination that may have remained after the initial light curve screening. The filtering was performed by fitting the spectral data to a model with components representing emission from the residual soft proton contamination, the target, the cosmic diffuse X-ray background, Gaussian lines, and solar wind charge exchange lines. The derived values of the spectral parameters for the soft proton contamination were then used in the ESAS task *proton* to create images of the soft proton contamination.

The analysis procedures described above created all of the primary components for a background-subtracted and exposure-corrected image. These components from all observations and three *XMM-Newton* detectors were then merged into a single image, weighting each detector by its relative effective area, and the resulting image adaptively smoothed. Following Ghirardini et al. (2018), the created image was also filtered by the *Chandra* tool *wavdetect* to detect and remove any remaining point sources and extended substructures that missed using the ESAS tool *cheese*. To create an adaptively binned image with binning the counts to at least 20 per energy bin, we applied a Voronoi tessellation algorithm (Diehl & Statler 2006) on the mosaicked count image.

Fig. 1 shows the spatial coverage of our *XMM-Newton* mosaicked and Voronoi tessellated image of the Coma cluster in the 0.7–1.2 keV energy band. We chose this energy range in order to minimize the high-energy-particle background, which rises significantly at low and high energies. The X-ray structure shows that the ICM gas in Coma extends in the west and southwest directions towards the infalling substructure NGC 4839.

The imaging-data analysis of galaxy clusters is subject to various sources of systematic uncertainty. The choice of the local background region, particularly at the cluster outskirts, is the major source of systematic uncertainty in the X-ray image of a galaxy cluster. For this purpose, we chose three background regions in three different locations outside the r_{200} radius of Coma, as shown in the magenta regions in Fig. 1, to extract the local X-ray background counts. The magenta region in the northwest is chosen as the local background for the cluster’s regions located in the west and northwest directions, and the one in the southwest direction is chosen as the local background for the regions located in the southwest and south directions. For other regions, the magenta region in the northeast is chosen as the local background. Moreover, we considered a $\pm 5\%$ uncertainty of the background level as an additional uncertainty in the radial profile of the X-ray surface brightness to account for background fluctuations, and is added in quadrature to each annulus in the count rates. All measurements reported in this paper take account of the systematic uncertainties discussed above.

Zhuravleva et al. (2013) have found that the distribution of gas densities in a given region of the ICM is well described as a log-normal component describing the bulk of the gas, and a high density tail resulting from gas clumping. In order to accurately measure the clumping factor, we therefore need a sufficient number of Voronoi tessellated regions in each region we study to be able to resolve the shape of the surface brightness distribution into these two components (the log-normal distribution and the tail). We find that a minimum of 150 independent Voronoi regions is needed to be able to accurately resolve the shape of the surface brightness distribution to calculate the median, and we ensure that this threshold is met for all of the regions we study both here and in our sector analysis in section 5.

To derive surface brightness profile for our mosaicked image of the Coma cluster, we extracted counts in concentric annuli centered at the cluster centre, (RA, Dec.) = (12:59:42.44, +27:56:45.53) This is the same cluster center as used in Simionescu et al. (2013), which we use for consistency and is the location of the X-ray peak. We tested the effect of changing the central coordinate used, and found this to have no significant effect on our results. We excluded the region that contains the NGC 4839 substructure from our analysis (the white sector in Fig. 1). When extracting the radial profile of the surface brightness profiles, particularly in the outskirts of clusters, it is important to consider possible biases introduced by gas clumping, which become increasingly important near the virial radius (Walker et al. 2019). We estimated the level of gas clumpiness directly from the X-ray image by dividing the mean surface brightness to the median surface brightness in each annulus region, as illustrated in Eckert et al. (2015). The inferred clumping factor \sqrt{C} is shown in Fig. 2. Within r_{500} , the estimated values of the clumping factor are low and show a slight trend of increasing with radius. Beyond r_{500} , the clumping value increases to around 1.2, consistent with the range of values typically found in the outskirts (Eckert et al. 2015; Walker et al. 2019).

In the upper panel of Fig. 3, we show the azimuthal median of the background-subtracted surface brightness profile for Coma in the 0.7–1.2 keV energy band. The electron density, shown in

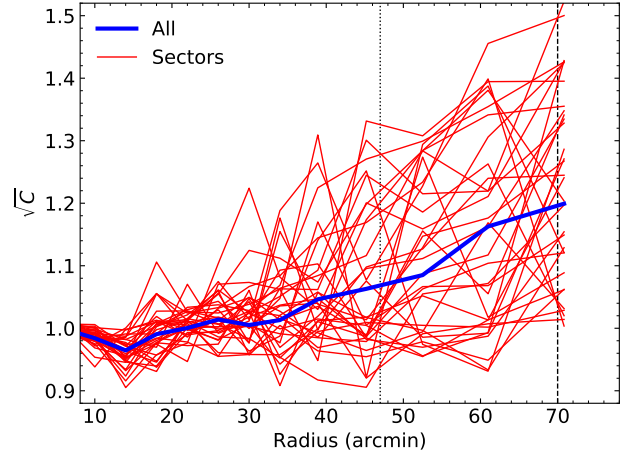


Figure 2. Radial profile of clumping factor for the azimuthally averaged profile (blue) and 33 angular sectors (red) discussed in Section 5. The vertical dotted and dashed lines represent the r_{500} and r_{200} radii, respectively.

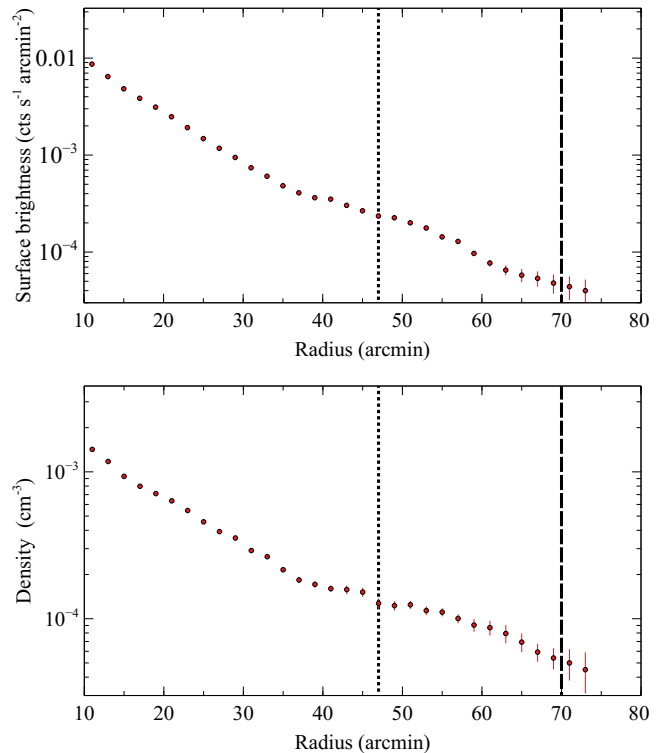


Figure 3. *Top:* Azimuthal median of the background-subtracted surface brightness profile for the Coma cluster in the 0.7–1.2 energy band. *Bottom:* Density profile obtained from the deprojection of the surface brightness radial profile using the onion peeling technique. The error bars are the 1σ percentiles computed using a Monte Carlo technique. The vertical dotted and dashed lines represent the r_{500} and r_{200} radii, respectively.

the lower panel of Fig. 3, was then recovered from the deprojection of median surface brightness profile using the onion peeling technique (Fabian et al. 1981; Kriss et al. 1983; Ettori et al. 2010), and assuming that the ICM plasma is spherical symmetry.

For the electron density, we follow the same approach as Tchermnin et al. (2016) and Ghirardini et al. (2019). We fold an APEC model (absorbed by the galactic column density, $N_{\text{H}} = 9.3 \times 10^{19} \text{ cm}^{-2}$ obtained from the Leiden-Argentine-Bonn survey, Kalberla

et al. 2005) through the *XMM-Newton* response in XSPEC to obtain the conversion between the count rate observed by *XMM-Newton* in the 0.7–1.2 keV band and the APEC normalization. As described in Tchernin et al. (2016), the 0.7–1.2 keV count rate is largely independent of temperature as long as the temperature is above ~ 1.5 keV. For consistency with Simionescu et al. (2013), we use the same abundance table (Grevesse & Sauval 1998) and the same metal abundance value in the outskirts of $0.3Z_{\odot}$. The APEC model normalization is related to the gas density as

$$\text{Norm} = \frac{10^{-14}}{4\pi[d_A(1+z)]^2} \int n_e n_H dV \quad (1)$$

where n_e and n_H are the electron and ion number densities respectively (which are related by $n_e = 1.17n_H$ in a fully ionized plasma, Grevesse & Sauval 1998), d_A is the angular diameter distance to the source, and z is the cluster redshift. From the deprojected APEC normalizations, we then calculated the density assuming spherical symmetry and a constant density in each shell, by calculating the projected volumes, V , of each shell in the 2D annuli.

3.2 Planck analysis

The *Planck* data used in this work are prepared by Planck Collaboration X (2013), using the Modified Internal Linear Combination Algorithm (MILCA). As in the analyses of the Tchernin et al. (2016), Ghirardini et al. (2018), and Ghirardini et al. (2019), we use only the high frequency channels from 100 to 857 GHz owing to the much larger PSF of the low frequency *Planck* channels. Fig. 4 shows the Comptonization parameter y map of the Coma cluster, obtained from a combination of *Planck* channels from 100 to 857 GHz. The y map has an effective PSF corresponding to 10 arcmin (FWHM), and a noise level of 2.3×10^{-6} . The *Planck* y map also shows the gas extends in the west and southwest directions, and the SZ effect signal is clearly detected towards the NGC 4839 substructure. Similar to the X-ray analysis, we excluded this region in our SZ analysis.

The dimensionless Comptonization parameter y , which determines the strength of interaction between the cosmic microwave background (CMB) photons and the hot ICM gas, is proportional to pressure, P , of the ICM gas integrated along the line of sight:

$$y = \frac{\sigma_T}{m_e c^2} \int P(l) dl, \quad (2)$$

where σ_T is the Thomson scattering cross-section, m_e is the electron mass, c is the speed of light, and the integration is taken over the line of sight l .

Following Planck Collaboration X (2013), the pressure profile of Coma was recovered by fitting the projected y radial profile to the universal pressure formula proposed by Nagai et al. (2007):

$$P(x) = \frac{P_0}{(c_{500}x)^\gamma [1 + (c_{500}x)^\alpha]^{(\beta-\gamma)/\alpha}}, \quad (3)$$

where $x = r/r_{500}$, P_0 is the normalization parameter, c_{500} is the concentration parameter defined at the characteristic radius r_{500} , and the parameters (γ, α, β) are respectively slopes in the central ($x \ll 1/c_{500}$), intermediate ($x \sim 1/c_{500}$), and outer ($x \gg 1/c_{500}$) regions.

For the fitting processes, we used the affine-invariant ensemble sampler for Markov chain Monte Carlo implemented in the *emcee* package (Goodman & Weare 2010). We let all five parameters in equation (3) free to vary. Our estimated values of the best-fitting parameters are statistically consistent with those obtained from the

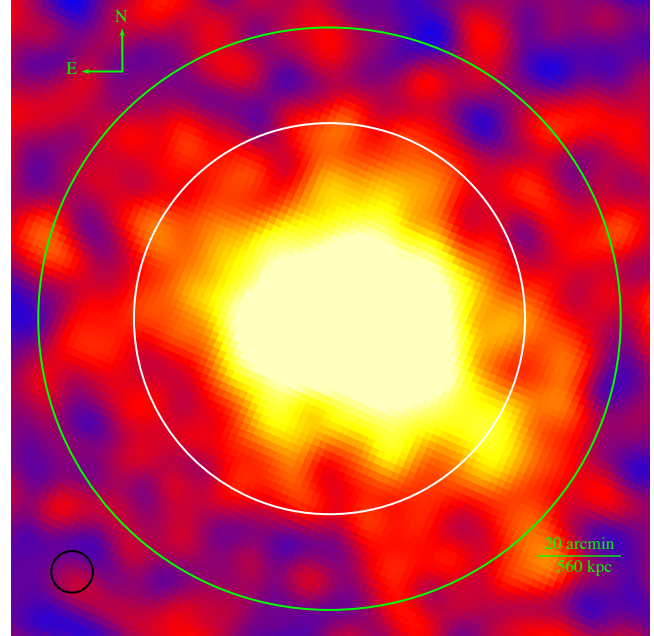


Figure 4. *Planck* y map of the Coma cluster, obtained by combining the *Planck* frequency channels from 100 to 857 GHz. The white and green circles represent the location of r_{500} and r_{200} , respectively. The black circle in the bottom left corner indicates the *Planck* beam size of 10 arcmin, which corresponds to a physical size of 280 kpc.

best-fitting model, Model C, reported by Planck Collaboration X (2013). The value of the reduced χ^2 associated with this fit is 1.06 with 9 degrees of freedom. Fig. 5 presents the best-fitting y model to the data and the pressure from the best-fitting parameters. We note that the model accurately reproduces the data over the entire radial range of the cluster. We take into account the covariance matrix between *Planck* data points, though this effect is small due to the large size of our bins.

4 JOINT X-RAY AND SZ EFFECT ANALYSIS

The electron density profile recovered from the X-ray observations (Section 3.1) and the pressure profile obtained from the SZ effect measurements (Section 3.2) can be combined to obtain the gas temperature, entropy, masses, and gas mass fraction profiles.

The temperature profile of the Coma cluster, as shown in the upper panel of Fig. 6, was recovered by dividing the pressure profile from *Planck* by the electron density from the deprojection of the *XMM-Newton* surface brightness profile. As we note, the temperature decreases from about 7.0 keV at a radius of 10 arcmin to about 3.0 keV at 70 arcmin.

Similarly, we were able to recover the entropy profile through the gas pressure and density profiles as

$$K = \frac{P}{n_e^{5/3}}. \quad (4)$$

In the lower panel of Fig. 6, we present our measurements of the azimuthally averaged entropy profile of the Coma cluster.

The radial profile of the gas entropy is of particular interest since it tracks the thermal history of a galaxy cluster. Numerical simulations (Voit et al. 2005) predicted that, in the absence of the radiative processes, the entropy profile outside the cluster core fol-

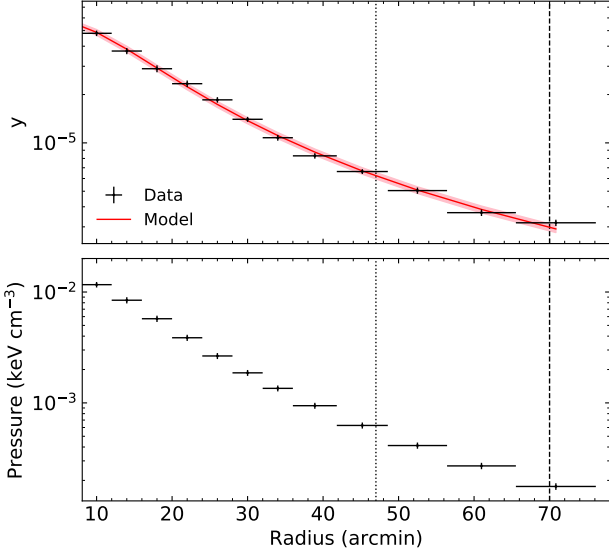


Figure 5. *Top:* Azimuthally averaged y profile of the Coma cluster with the best-fitting model. *Bottom:* Pressure profile predicted from the best-fitting parameters. The shadow pink area indicates the 68.3 per cent confidence intervals obtained by MCMC simulations, and the vertical dotted and dashed lines represent, respectively, the r_{500} and r_{200} radii.

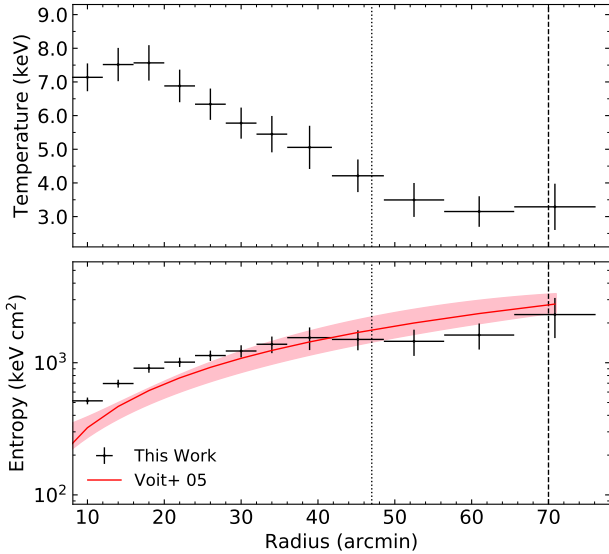


Figure 6. Temperature (*top*) and entropy (*bottom*) profiles of the Coma cluster obtained by combining the X-ray density and SZ pressure measurements. The red solid line indicates the entropy predicted by Voit et al. (2005). The shaded pink area represents the region enclosed by the median profile and scatter of the non-radiative simulations in Voit et al. (2005). The vertical dotted and dashed lines represent, respectively, the locations of the r_{500} and r_{200} radii. We plot using a linear radial axis to emphasize the outskirts.

lows a power law with characteristic slope of 1.1,

$$\frac{K}{K_{500}} = 1.47 \left(\frac{r}{r_{500}} \right)^{1.1}, \quad (5)$$

where

$$K_{500} = 106 \text{ keV cm}^2 \left(\frac{M_{500}}{10^{14} M_{\odot}} \right)^{2/3} E(z)^{-2/3} f_b^{-2/3}, \quad (6)$$

M_{500} is the cluster mass at r_{500} , $E(z)$ describes the redshift evolution of Hubble parameter, and f_b is the universal baryon fraction and assumed to be equal to 0.15 (following Pratt et al. 2010).

The predicted entropy profile from this power-law relation is overlotted together with the measured entropy profile in the lower panel of Fig. 6. We see a clear excess in the entropy measured in the central region of the cluster out to a radius of about 30 arcmin. However, the recovered entropy is consistent with the expected trend at radii between 30-50 arcmin. Beyond 50 arcmin, although it has a shallower slope, the recovered entropy is statistically in agreement with the baseline entropy profile predicted by the numerical simulations (Voit et al. 2005) given the scatter in the simulated entropy profiles.

To calculate the gas mass, we integrated the density profile over a given volume, and then multiplied by the mean mass per electron, $\mu_e m_p$. The gas mass can be expressed as

$$M_{\text{gas}} = 4\pi\mu_e m_p \int n_e(r) r^2 dr, \quad (7)$$

where the limit is taken out to some cut-off radius. The total mass of the cluster, which is mainly made up of the dark matter, can be deduced from the gas structure. Its distribution relates to the pressure profile of the ICM gas. Assuming that the gas is in the hydrostatic equilibrium in the gravitational potential well of the cluster with no significant flow of matter, the total mass takes the form:

$$M_{\text{tot}} = - \frac{r^2}{G\mu_e m_p n_e(r)} \frac{dP(r)}{dr}, \quad (8)$$

where G is the Newtonian gravitational constant, and the pressure term satisfies the ideal gas law.

Both gas and total masses were calculated using the following method. We used a four-point spline interpolation to compute the integral in equation (7), and a three-point quadratic interpolation for the pressure derivative in equation (8). The gas mass fraction is then recovered as $f_{\text{gas}} = M_{\text{gas}}/M_{\text{tot}}$.

Fig. 7 presents the gas mass, total mass, and gas mass fraction profiles of the Coma cluster out to the virial radius. As a general trend, these measurements increase radially with increasing radius, and reach the maximum value at the cluster outskirts. The estimated total mass of Coma at r_{200} ($= 2.0$ Mpc) is $(8.50 \pm 0.55) \times 10^{14} M_{\odot}$. This value is in excellent agreement with the M_{200} value from the $Y_X - M$ scaling relation obtained in Planck Collaboration X (2013) of $8.6 \times 10^{14} M_{\odot}$. Our measurements for the azimuthally averaged gas mass fraction at r_{200} are also statistically in agreement with the universal baryon fraction of 0.156 ± 0.003 reported by Planck Collaboration XIII (2016).

5 AZIMUTHAL SECTOR ANALYSIS

Taking advantage of our high-quality data from both X-ray and SZ effect observations, we can apply the analysis described in the previous sections on smaller regions of the Coma cluster. Ghirardini et al. (2018) found when performing their joint XMM and Planck analysis on the cluster Abell 2319 (which has $r_{200} = 32$ arcmin) that they could divide Abell 2319 into 8 sectors to assess the azimuthal variations in thermodynamic properties. Coma's much larger spatial extent allows us to dramatically increase the number of sectors into which it can be resolved by *Planck*. The Coma cluster (with $r_{200} = 70$ arcmin) covers an area that is $(70/32)^2 = 4.8$ times greater than that of Abell 2319, so we can increase the number of sectors in our analysis of the azimuthal variations in Coma by

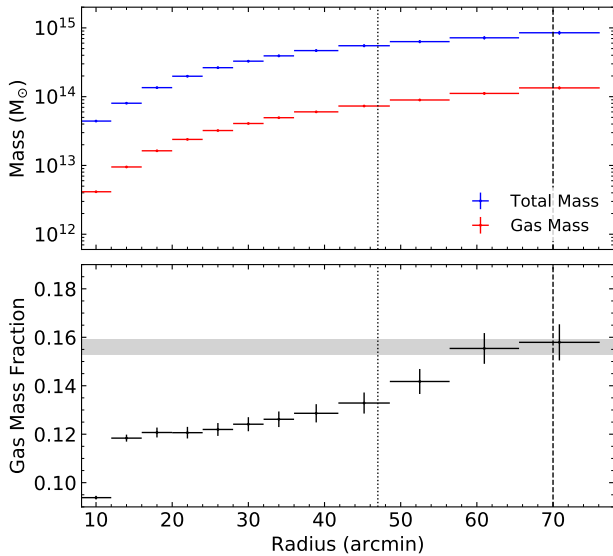


Figure 7. *Top:* Gas and total mass profiles of the Coma cluster. *Bottom:* Azimuthally averaged gas mass fraction of Coma. The gray shadow area represents the *Planck* universal baryon fraction (Planck Collaboration XIII 2016). The vertical dotted and dashed lines mark the positions of the r_{500} and r_{200} radii, respectively.

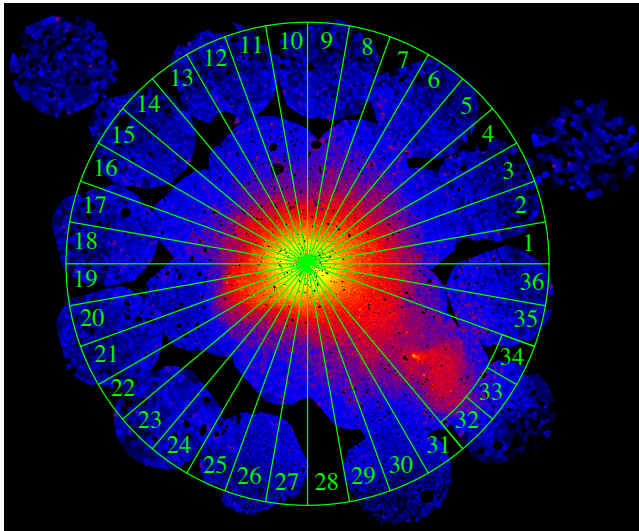


Figure 8. Locations of the 36 azimuthal sectors overlaid on the X-ray image of the Coma cluster. Similar to the azimuthally averaged analysis, we excluded the region in the southwest direction where the substructure NGC 4839 is located. Any gaps in the mosaic have been linearly interpolated over, and the values for the missing sector 28 are tied to those of sector 29.

this factor to $8 \times 4.8 = 38.4$. For simplicity, and to make the presentation of our results intuitive, we divide our analysis in 36 sectors (since there are 360 degrees in a circle). We find 36 to be the optimum number of sectors, as having more sectors would mean we have too few Voronoi tessellated regions to measure the clumping factor accurately in each sector, while using fewer sectors would be under-utilizing the data. When binning each sector radially to form profiles, we ensure that we have enough independent Voronoi tessellated regions in each radial bin we study to accurately measure the clumping bias (as discussed earlier in Section 3.1). In the small number of sectors where the XMM coverage in the outskirts

is low (sectors 1 and 4 and 34), we use the clumping values from their neighbouring sectors. The analysis in azimuthal sectors allows us to measure the variations in the thermodynamic properties of the Coma cluster out to the virial region. In this analysis of the sectors, any small gaps in the XMM mosaic are linearly interpolated over.

Fig. 8 shows the locations of the azimuthal sectors where the X-ray and SZ effect data were extracted and analysed. Each of the 36 azimuthal sectors has an angular width of 10 degrees and extends up to the r_{200} radius. For sector 28, where there is no X-ray coverage in the outskirts, we tie the X-ray surface brightness to be that same as that in the adjacent sector 29. Along the southwest direction, where the bright subgroup NGC 4839 is located, we excluded the region that covers the cluster core up to a radius of 60 arcmin, so as to exclude the emission from NGC 4839 and its tail. The recovered temperature and entropy along this direction outside 60 arcmin (sectors 32, 33, and 34) are shown in Fig. 14. All measurements presented in this section take account of the systematic uncertainties discussed in Section 3.1, and corrected for gas clumping (see Fig. 2).

The density profiles in the azimuthal sectors, as shown in Fig. B1, exhibit a small scatter from the averaged density profile in the central region of the cluster, but scatter is more significant outward towards the cluster outskirts, agreeing with the prediction of cosmological simulations (e.g. Nelson et al. 2014). Some azimuthal sectors show an excess gas density in the outskirts region beyond r_{500} , compared to the azimuthally averaged density profile. This excess, however, is significantly higher beyond a radius of 40 arcmin in sectors that lie between south and west. Apart from this excess, the gas density profiles in some sectors that lie between east and south drop sharply between 30-40 arcmin and then flat out at radii between 40-50 arcmin. As found in Brown & Rudnick (2011), the edge of this sharp drop in the gas density agrees well with the outermost edge of the giant radio halo observed with the Westerbork Synthesis Radio Telescope (WSRT, shown in Fig. 17).

The pressure profiles in the azimuthal sectors, obtained by fitting the projected y profile in each sector to the universal pressure profile (equation 3), are shown in Fig. B2. Like the density profile, we see a small scatter from the averaged pressure profile in the central region of the cluster, but increases radially with the cluster radius, although smaller than that for the density profiles.

In Fig. 9, we show the temperature profiles in the azimuthal sectors recovered from the density and pressure measurements. In this figure, we also show the azimuthally averaged temperature profile. As a general trend, the temperature profiles in most azimuthal sectors exhibit broadly consistent radial trends, with the gas temperature dropping from about 8.0 keV at a radius of 10 arcmin to about 3.0 keV in the cluster outskirts, with few exceptions. For instance, the temperature measurements in sectors 10-18 (the north east of the cluster) are, on average, higher than the azimuthally averaged profile over the most cluster radial range. In contrast, in the azimuthal sectors that lie between east and south, the temperature measurements are, on average, lower than the azimuthally averaged profile from the cluster centre out to the cluster outskirts. A temperature map of the central 40 arcmin of Coma region is shown in Fig. 10, showing the north/south asymmetry in the temperature. Our results agree well with the hot north and colder south observed in the central regions with *Chandra* in Sanders et al. (2013), and show that this asymmetry extends to much around 30-40 arcmin.

In sectors to the south-west, the temperature profiles are statistically below the azimuthally averaged temperature profile from the centre of the cluster out to about 20 arcmin. From about 20-50 arcmin, the temperature profiles show a drop from about 6.0 keV

to about 2.0 keV. Beyond r_{500} , however, the temperature profiles along these sectors decline only slightly with radius or remain unchanged.

The entropy profiles in the azimuthal sectors are shown in Fig. 11. We plot these profiles using a linear radial axis to emphasise the outskirts regions. In this figure, we show the azimuthally averaged profile along with the power-law entropy profile predicted by non-radiative simulations (Voit et al. 2005). Within a radius of 30 arcmin, the entropy profiles along most azimuthal sectors, on average, exhibit an apparent excess with respect to the power-law profile predicted by non-radiative simulations. Beyond a radius of 30 arcmin, the entropy profiles show a better agreement with the power-law behavior predicted from simulations. However, in the south-western quarter of the cluster, the entropy flattens and deviates significantly below the predicted profile. For sectors that lie between north and east, in contrast, we see an apparent entropy excess along several sectors out to the outskirts, implying the presence of merger activities which is likely associated with infalling subgroups (Simionescu et al. 2013).

The entropy map of the outskirts is shown in Fig. 12. The low entropy region to the south west coincides with the western filament connecting the Coma cluster to the cosmic web found in Malavasi et al. (2020), indicated by the green arrow in this figure. The locations of the filament galaxies found in Mahajan et al. (2018) are plotted as the green points on Fig. 12, showing a strong correlation between the size and location of this cosmic web filament, which has a width around 2 Mpc, and the entropy decrement in the south western quadrant.

We also computed the gas and total mass profiles in the azimuthal sectors using the same methods (see Figs. B3 and B4). From these mass measurements, the gas mass fraction profile is then recovered for all azimuthal sectors. In Fig. 13, we show the gas mass fraction profiles in the azimuthal sectors, along with the azimuthally averaged profile and the universal baryon fraction measurement reported by Planck Collaboration XIII (2016). As a general trend, the results indicate that the computed gas mass fractions increase slightly with a radius within the central and intermediate radii of the cluster and then tend to flat out at larger radii. However, this is not the case in every azimuthal sector. For example, the gas mass fraction measurements in some sectors that lie between north and west are significantly high at the cluster centre, indicating that the total mass in these sectors may be underestimated as a result of the presence of the possible non-thermal pressure component in the cluster core. However, the gas mass fraction profiles along these sectors drop outward, in better agreement with the universal baryon fraction at larger radii. In the south western quadrant, the gas mass fraction in the outskirts is found to be far higher, well in excess of the mean cosmic baryon fraction.

5.1 Azimuthal scatter profiles

In Fig. 14, we plot the azimuthal variation of the temperature and entropy in the outermost two annuli. We see clear azimuthal variation in the entropy, which is systematically lower in the south west direction, between sectors 27 and 36.

To investigate the level of asymmetry in the radial profiles of the thermodynamic quantities recovered from X-ray and SZ effect observations in more detail, we computed the azimuthal scatter (Vazza et al. 2011; Ghirardini et al. 2018) in all sectors with respect to the azimuthally averaged profile. For a given number of sectors

N , the azimuthal scatter is defined at each radius r as

$$\sigma_q(r) = \sqrt{\frac{1}{N} \sum_{i=1}^N \left(\frac{q_i(r) - \bar{q}(r)}{\bar{q}(r)} \right)^2}, \quad (9)$$

where $q_i(r) = \{C, n_e, P, T, K, M_{\text{gas}}, M_{\text{tot}}, f_{\text{gas}}\}$ in sector i , and $\bar{q}(r)$ is the azimuthally averaged profile taken over the entire cluster volume.

The scatter in the radial profiles of the recovered thermodynamic quantities of the Coma cluster is shown in Fig. 15. A small value of $\sigma_q(r)$ implies no significant deviations from spherical symmetry, while a large $\sigma_q(r)$ indicates a very asymmetric gas. Overall, the azimuthal scatter $\sigma_q(r)$ of the recovered thermodynamic quantities increases towards the cluster outskirts, in agreement with the predictions of cosmological simulations. The scatter in the temperature and density in the r_{500} to r_{200} is in the range 0.2-0.3, in good agreement with the range found in the simulations of Vazza et al. (2011).

Although this is a general trend, there are a few exceptions. For example, the gas mass fraction exhibits a significant scatter in the central region of the cluster. Such large scatter might indicate that the total mass is underestimated within the central region of the cluster, supporting the presence of significant non-thermal pressure component in the core. The presence of such pressure is highly likely in this non-cool-core system and has previously been reported (see Neumann et al. 2003; Schuecker et al. 2004; Simionescu et al. 2013, for example). Furthermore, there is a particular location near a radius of 40 arcmin where we observe a significant jump in the azimuthal scatter of the gas temperature and entropy. This location coincides well with the outermost edge of the giant radio halo observed at 352 MHz with the WSRT.

5.2 Comparison with *Suzaku*

In Fig. 16, we compare our temperature and entropy measurements with those obtained using *Suzaku*, reported by Simionescu et al. (2013). Our measurements are extracted in the same regions as the *Suzaku* observations to allow a fair comparison of the measurements. We find that there is good agreement between our temperature and entropy measurements between the two different methods. Our slightly higher entropies in the outskirts are to be expected as our gas densities have been corrected for gas clumping.

6 DISCUSSION

In this work, we combined the gas density measurements obtained from the deprojection of the surface brightness radial profile using *XMM-Newton* observations with the gas pressure measurements obtained through the SZ effect signal using the *Planck* observatory. The radial profiles of the thermodynamic properties of the Coma cluster were recovered out to the virial radius with nearly full azimuthal coverage for the first time. Furthermore, our high-quality data allowed us to investigate in detail the thermodynamic properties of the ICM gas out to the Coma outskirts in the 36 azimuthal sectors. This has enabled us to produce the most complete high-resolution view of the thermodynamic properties of the outskirts of a galaxy cluster ever achieved.

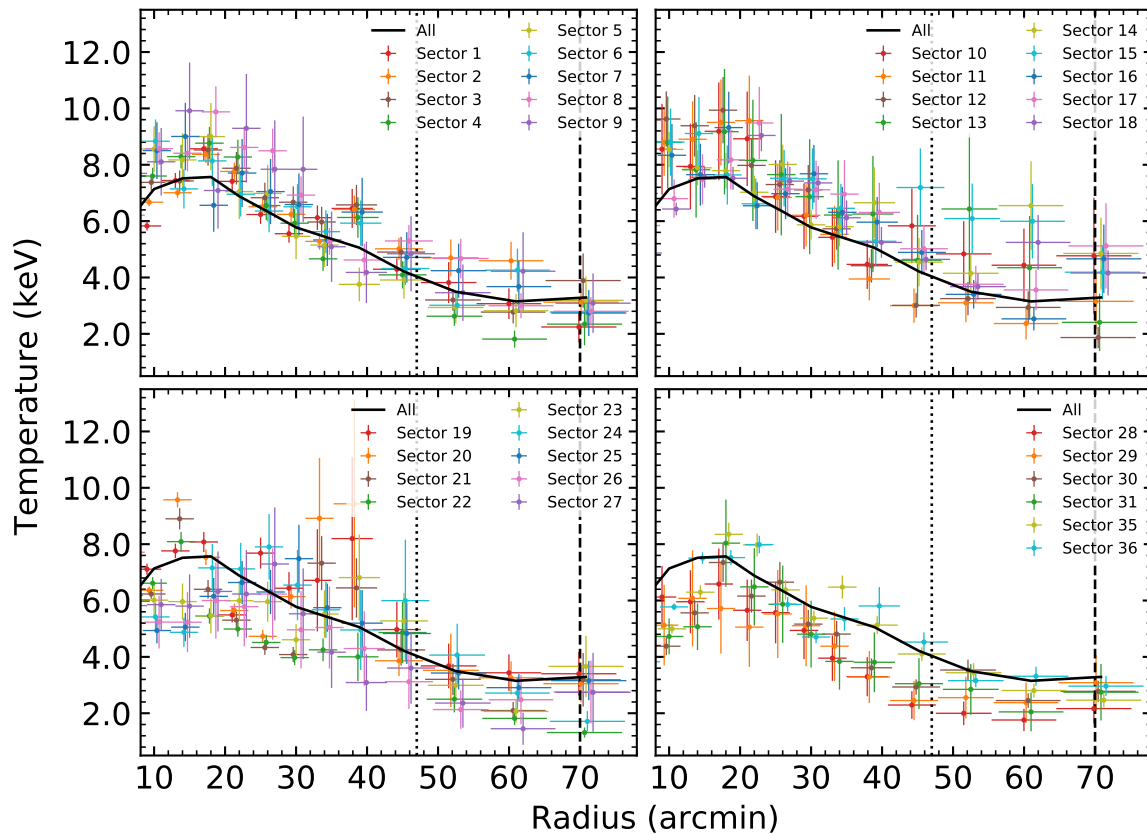


Figure 9. Temperature profiles in the azimuthal sectors of the Coma cluster obtained from combining the X-ray density and SZ pressure measurements. The error bars are the 1σ percentiles computed using a Monte Carlo technique. The thick black line shows the azimuthally averaged temperature profile. The vertical dotted and dashed lines mark the positions of the r_{500} and r_{200} radii, respectively. We introduce small offsets between data points at the same radius to aid readability.

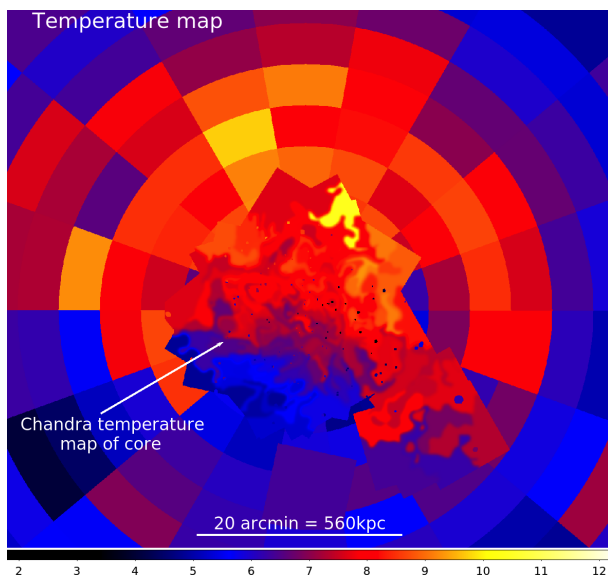


Figure 10. Temperature map of the central regions of Coma from the joint *XMM/Planck* analysis (sectors) compared to the *Chandra* temperature map of the core from Sanders et al. (2013). The asymmetry between the hotter northern region and cooler southern region found in the core with *Chandra* is found to extend out to much larger radius.

6.1 Complex morphology of Coma

It is well established that the Coma cluster is an unrelaxed system, with a number of substructures which we summarize here and show in Fig. 17. Lyskova et al. (2019) have argued that the morphology of the infalling group NGC 4839 is best explained if it has fallen from the north east and already passed by the Coma centre, and is returning from the southwest direction. On the other hand, previous work (e.g. Neumann et al. 2001, Akamatsu et al. 2013) has suggested that it is falling into Coma for the first time.

Coma features two brightest cluster galaxies in its central regions, NGC 4874 and NGC 4889 (Sanders et al. 2014), which appear to be in their final stage of the merging process (Coccatto et al. 2010). Vikhlinin et al. (1997) have reported on a 1 Mpc long excess in X-ray surface brightness extending from the core to the south east direction towards the galaxy NGC 4911.

The Coma cluster hosts a giant radio halo (Coma C; Willson 1970) extending over scales of about 1 Mpc (≈ 36 arcmin) and traces the non-thermal emission from relativistic electrons and magnetic fields (see Fig. 17). The Coma cluster also appears to have at least two shock fronts (Planck Collaboration X 2013) in two regions about 40 arcmin to the west and the southeast of the cluster centre (marked in Fig. 17), corresponding to the outermost edge of the giant radio halo.

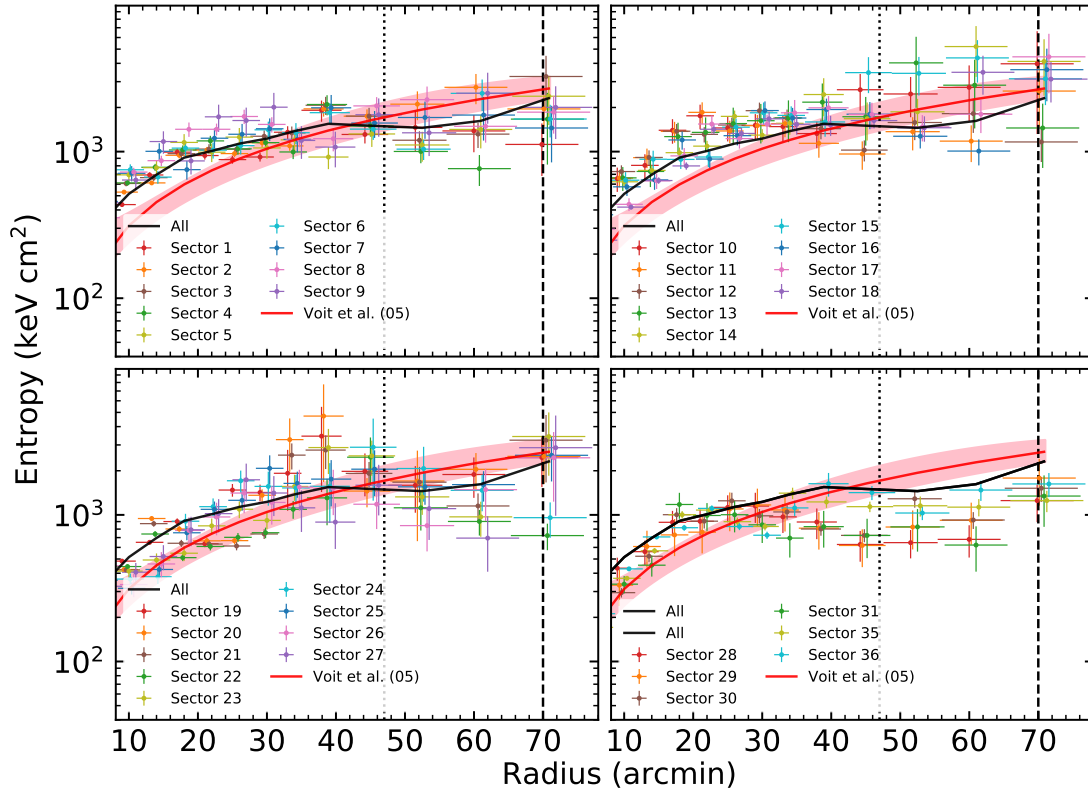


Figure 11. Same as Fig. 9, except for entropy. The red solid line indicates the entropy predicted by Voit et al. (2005). The shaded pink area represents the region enclosed by the median profile and scatter of the non-radiative simulations in Voit et al. (2005).

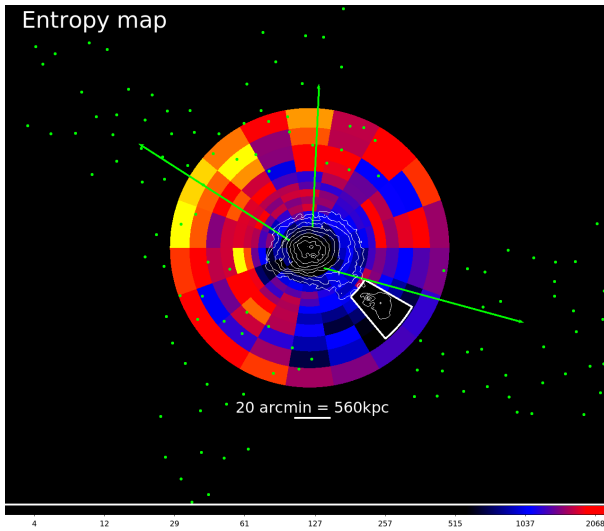


Figure 12. Wide-scale entropy map of the Coma cluster from the joint *XMM/Planck* analysis. The white contours show the brightest X-ray features. The thick white sector around the merging group NGC 4839 is excluded from the map. The green arrows show the direction of the cosmic web filaments found in Malavasi et al. (2020) that connect the Coma cluster to neighbouring galaxy clusters. The filament galaxies from Mahajan et al. (2018) are shown as the green dots. We see that the south western area has systematically lower entropy than the rest of the cluster, possibly indicating the presence of a filamentary gas stream of low entropy gas, extending deep into the Coma cluster in this direction. Any gaps in the mosaic have been linearly interpolated over, and the values for the missing sector 28 are tied to those of sector 29.

6.1.1 Structure outside r_{500}

In the south western direction, we have found that there is a clear entropy deficit (in the range $2-3\sigma$) below the baseline entropy profile from $0.5r_{200}$ outwards, and extending from sectors 27 to 36 (a quarter of the cluster azimuth) as shown in the entropy profiles in Fig. 11 and the entropy map in Fig. 12. The extent of this entropy decrement is far larger than the size of the infalling group NGC 4839, which we exclude from our analysis.

This direction coincides with a where a cosmic web filament joins the Coma cluster, connecting it to Abell 1367 to the west (Malavasi et al. 2020). The locations of the filament galaxies surrounding the Coma cluster found in Mahajan et al. (2018) are shown as the green dots in Fig. 12. Fig. 12 shows that the width and location of the galaxy distribution in the western filament is consistent with the size of the low entropy south western sector in Coma. This low entropy is consistent with what is expected for a penetrating filamentary gas stream (Zinger et al. 2016), which can bring low entropy gas deep into central regions of the cluster.

Malavasi et al. (2020) also report on two other cosmic web filaments connecting to the Coma cluster to the north and north east (shown by the green arrows and the galaxy distribution in Fig. 12), however we find no entropy decrement in those directions. As described in Zinger et al. (2016), the penetration of the gas streams into the cluster interior as the cluster ages can vary depending on a range of factors such as the mass inflow rate along the filament. In some cases filaments that once penetrated into the cluster core can weaken and be ‘pushed out to radii greater than the virial radius. It is therefore possible that the south western filamentary gas stream has been able to penetrate deeper into the cluster than the other two

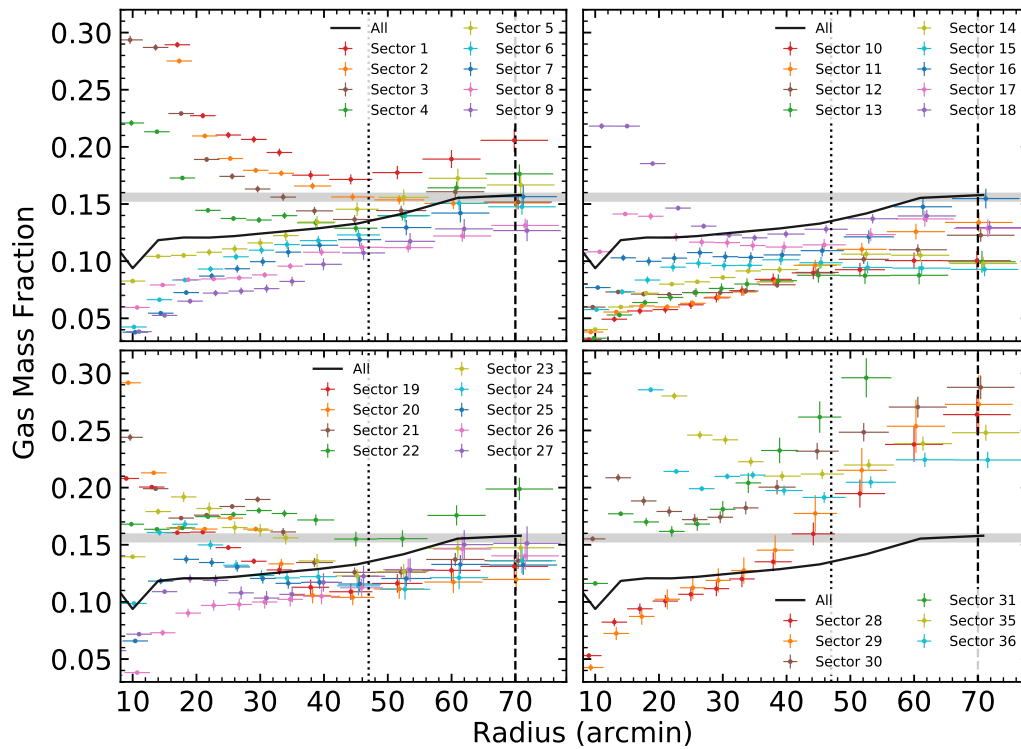


Figure 13. Same as Fig. 9, except for the gas mass fraction. The gray shadow area represents the *Planck* universal baryon fraction (Planck Collaboration XIII 2016).

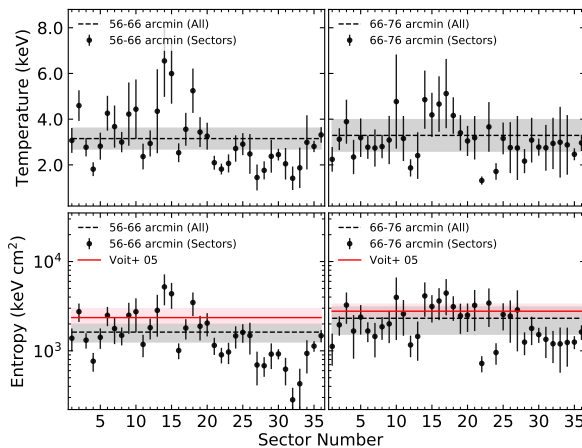


Figure 14. Azimuthal variation in the gas temperature (*top*) and entropy (*bottom*) in the last two annuli for all 36 azimuthal sectors. The dotted lines are the azimuthally averaged temperature (*top*) and entropy (*bottom*), omitting the sectors coincident with the merging group NGC 4839 (sectors 32 to 34). The shaded gray regions represent 1σ uncertainty. The red solid line indicates the entropy predicted by Voit et al. (2005). The shaded pink region corresponds to the region enclosed by the median profile and scatter of the non-radiative simulations in Voit et al. (2005).

filaments, possibly due to the mass inflow rate being higher along the south western filament.

Zinger et al. (2016) also find in their simulations that deeply penetrating gas streams can carry large amounts of momentum and energy into the cluster core, driving random motions and keeping the cluster in an unrelaxed dynamical state. It is possible that the deeply penetrating accretion along the south western filament in

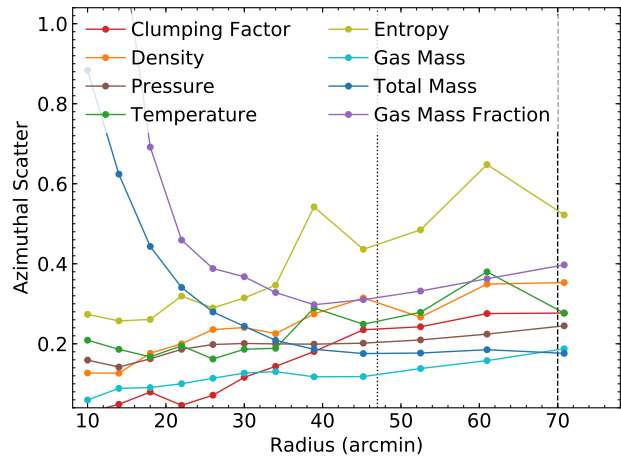


Figure 15. Azimuthal scatter in the radial profiles of the thermodynamic quantities of the Coma cluster recovered from X-ray and SZ effect observations. A small value of azimuthal scatter means no significant deviations from spherical symmetry, while a large azimuthal scatter suggests an asymmetric gas. The vertical dotted and dashed lines show the positions of the r_{500} and r_{200} radii, respectively.

the Coma cluster is at least partly responsible for keeping it in an unrelaxed (non cool core) state.

6.1.2 Inside r_{500}

Our measurements within a radius of 30 arcmin from the cluster centre, on average, show a temperature gradient from the hotter northwest region to the colder region in the southeast, in agreement with previous studies (e.g. Watanabe et al. 1999; Neumann et al.

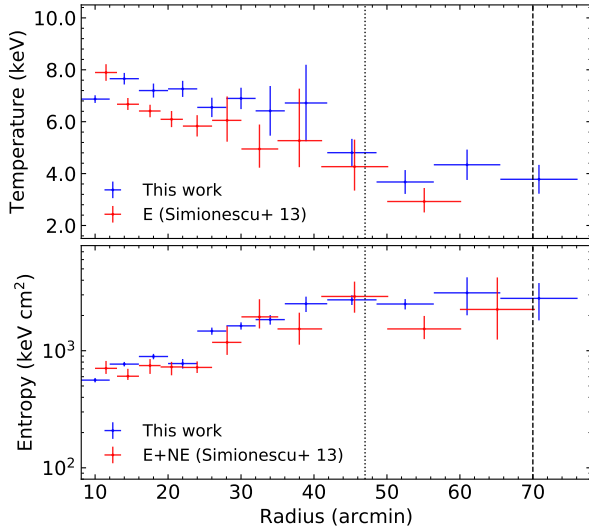


Figure 16. Comparing the Suzaku measurements of the temperature (*top*) and entropy (*bottom*) from Simionescu et al. (2013) obtained along strips with the profiles along the same sectors found in this work. The error bars are the 1σ percentiles computed using a Monte Carlo technique. The vertical dotted and dashed lines mark the positions of the r_{500} and r_{200} radii, respectively.

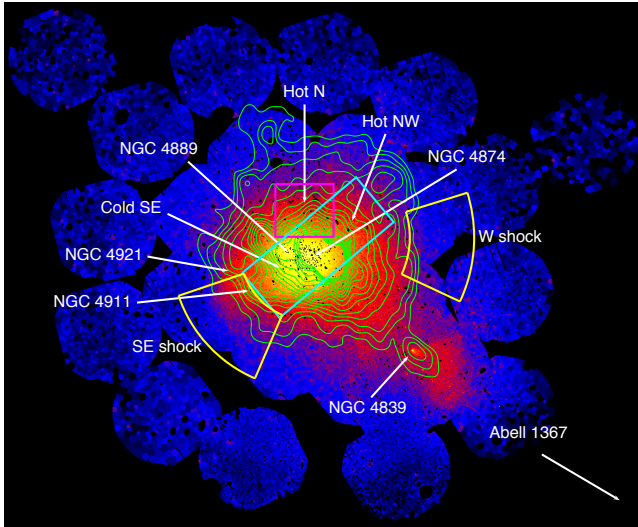


Figure 17. *XMM-Newton* image of the Coma cluster with the 352 MHz WSRT radio contours from Brown & Rudnick (2011) are overlaid. It shows the locations of the substructures and features of the cluster discussed in the main text.

2003; Sato et al. 2011; Sanders et al. 2013). In Fig. 10, we show the temperature map of the central region of Coma from our joint *XMM/Planck* analysis, and compare it to the *Chandra* temperature map of the core from Sanders et al. (2013). The asymmetry between the hotter northern region and cooler southern region found in the core with *Chandra* is found to extend out to much larger radius.

Watanabe et al. (1999) and Neumann et al. (2003) argued that the hot region in the northwest is due to shock waves induced by the infall of a small substructure around NGC 4874 to the main body of the Coma cluster from the southeast direction. On the other hand, the cool gas in the southeast region, particularly near 25 arcmin, shows a significant drop in the entropy profile, relative to the av-

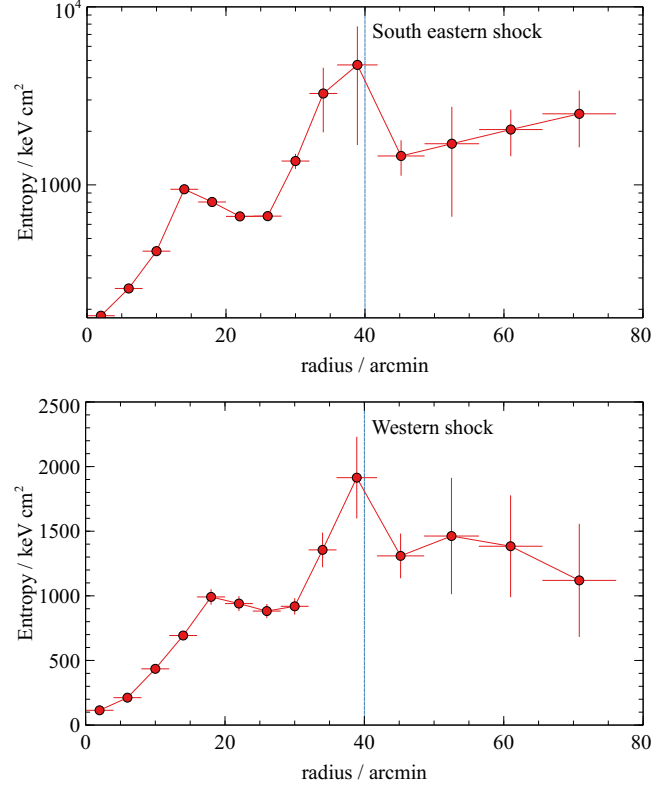


Figure 18. Entropy profiles along the directions of the South Eastern (*top*) and Western (*bottom*) shocks, showing the entropy jump behind the shock locations, which are marked by the vertical dashed line

eraged profile, which seems to be mainly caused by the enhanced gas density in the region. Sanders et al. (2013) argue that the cool gas in this region is likely stripped from the infall of a small group, consisting of low-entropy material, centered near the two galaxies NGC 4921 and NGC 4911.

Donnelly et al. (1999) and Neumann et al. (2003) observed a hot region within a radius of 30 arcmin to the north from the centre of the Coma cluster (Fig. 9, upper panels) using *ASCA* and *XMM* respectively. Our results confirm the existence of this hot spot, as reported by these authors. In the same region, we also observe an apparent entropy excess (Fig. 11, upper panels) and a low gas mass fraction compared with other regions (Fig. 13, upper panels). It was argued that this region is heated by a shock wave created by a previous merger from a small group centered near the galaxy NGC 4889, which is currently one of the two dominant galaxies in the core of the Coma cluster.

As expected from the shocks observed by Planck Collaboration X (2013) to the south-east and west, at radii between 30-40 arcmin, the southeastern sectors show a jump in the gas temperature (Fig. 9, lower left) and entropy at the 1σ level (Fig. 11, lower left and also Fig. 18 in which we show just the entropy profiles in the directions of the shocks). At the same radii, the radial profile of the gas density along these sectors shows a sharp drop (Fig. B1, lower left). A similar trend is also seen in the thermodynamic properties at the same radii along the western sectors. The structure at 10-15 arcmin to the SE is caused by a linear feature near the core that has been studied in depth in previous works (e.g. Sanders et al. 2013).

7 CONCLUSIONS

In this work, we have presented our new extended *XMM-Newton* mosaic of the Coma cluster, which covers the cluster out to r_{200} with nearly complete azimuthal coverage. By combining the gas density measurements obtained from the X-ray surface brightness profile of this mosaic with the gas pressure measurements obtained via the SZ effect signal using *Planck*, we have able to recover the thermodynamic properties of the Coma cluster out to the virial radius with nearly full azimuthal coverage for the first time. Furthermore, our high-quality X-ray and SZ effect data have allowed us to investigate in detail the thermodynamic properties of the ICM out to r_{200} in 36 azimuthal sectors. This has enabled us to produce the highest spatial resolution view of the thermodynamics of the entire outskirts of a galaxy cluster ever achieved.

Beyond r_{500} , the temperature profiles of the Coma cluster, on average, do not appear to drop sharply. The entropy profiles along the relatively less disturbed directions are statistically consistent with the baseline entropy profile predicted by cosmological simulations for purely gravitational hierarchical structure formation (Voit et al. 2005).

Our results show that the radial profiles of the thermodynamic quantities recovered from X-ray and SZ effect data become increasingly asymmetric in the outskirts, in agreement with the predictions of cosmological simulations of galaxy cluster formation (e.g. Avestruz et al. 2014; Lau et al. 2015).

We find that there is a significant entropy deficit from $0.5r_{200}$ out to the virial radius in the south western direction, which coincides with the direction of a cosmic web filament which connects the Coma cluster to Abell 1367 (Fig. 12). The entropy deficit extends for around a quarter of the cluster azimuth to the south west. The size of the entropy decrement is very similar to the width of the western filament as traced by its constituent galaxies (around 2 Mpc), and is much larger than the spatial scale of the infalling group NGC 4839 which we exclude from the analysis. This low entropy is consistent with theoretical expectations for filamentary gas streams originating from the cosmic web (e.g. Zinger et al. 2016), which can penetrate deep into the cluster interior, channeling low entropy gas.

The inner radius to which this entropy decrement extends is consistent with the radius of the western shock, 40 arcmin from the core. As remarked upon by Malavasi et al. (2020), who studied the filamentary large scale environment of Coma and observed that the western shock location coincides with the connection between Coma and the western filament, it is possible that this western shock is the result of accretion along the western cosmic web filament onto the Coma cluster.

The two other cosmic web filaments connecting to the Coma cluster to the north and northeast do not appear to have significantly disrupted the thermodynamics of the Coma cluster within the virial radius. It is possible that the mass inflow rate is much lower along those filaments, and that their gas streams are currently unable to penetrate into the central r_{200} of the cluster. Simulations (Zinger et al. 2016) have found the penetration of the gas streams associated with cosmic web filaments can vary substantially, with some penetrating deep into the central regions of clusters while other are unable to penetrate within the virial radius. If we are seeing a gas stream penetrating the Coma cluster to the south west, it is possible that the large amounts of energy and momentum it carries into the cluster is contributing to keeping Coma in an unrelaxed state.

At small and intermediate radii, our results confirm the existence of several complex features reported in the literature. The

measurements within a radius of 30 arcmin show a gradient in the gas temperature from the hotter northwest region to the colder region in the southeast, in agreement with previous studies (e.g. Watanabe et al. 1999; Neumann et al. 2003). These high temperature regions may be due to shock heating induced by the infall of a substructure around NGC 4874 to the cluster core from the south-east direction. Our observations also confirm the existence of a hot spot at the north side of the Coma core, which reported in previous studies using *ASCA* (e.g. Donnelly et al. 1999).

At radii between 30–40 arcmin, there is a jump in the gas temperature and entropy along the southeastern sectors. A similar trend is also seen in the thermodynamics at the same radii along the western sectors. These features correspond to the well known shock fronts (Planck Collaboration X 2013), and the edge of these features coincides with the edge of the giant radio halo observed at 352 MHz (Brown & Rudnick 2011).

Our results underline the enormous discovery space presented by the outskirts of galaxy clusters to new high throughput X-ray observatories such as *ATHENA* (Barcons et al. 2017), and proposed concepts such as *Lynx* (Gaskin et al. 2019) and *AXIS* (Mushotzky et al. 2019). A complete understanding of how galaxy clusters form and grow can only be achieved by pushing out to understand their outskirts and how they connect to the surrounding cosmic web (Walker et al. 2019, Bulbul et al. 2019, Simionescu et al. 2019).

ACKNOWLEDGEMENTS

We thank the referee for their helpful report. MSM and SAW acknowledge support from the NASA XMM-Newton grant 19-XMMNC18-0030. Based on observations obtained with XMM-Newton, an ESA science mission with instruments and contributions directly funded by ESA Member States and NASA. We thank Shea Brown for providing the radio contours shown in Fig. 17, and Jeremy Sanders for providing the central *Chandra* temperature map shown in Fig. 10.

DATA AVAILABILITY

The XMM-Newton Science Archive (XSA) stores the archival data used in this paper, from which the data are publicly available for download. The XMM data were processed using the XMM-Newton Science Analysis System (SAS). The software packages *heasoft* and *xspec* were used, and these can be downloaded from the High Energy Astrophysics Science Archive Research Centre (HEASARC) software web-page. Analysis and figures were produced using PYTHON version 3.7.

REFERENCES

- Akamatsu H., Inoue S., Sato T., Matsusita K., Ishisaki Y., Sarazin C. L., 2013, *PASJ*, 65, 89
- Arnaud M., Pratt G. W., Piffaretti R., Böhringer H., Croston J. H., Pointecouteau E., 2010, *A&A*, 517, A92
- Avestruz C., Lau E. T., Nagai D., Vikhlinin A., 2014, *ApJ*, 791, 117
- Barcons X., Barret D., Decourchelle A., den Herder J. W., Fabian A. C., Matsumoto H., Lumb D., Nandra K., Piro L., Smith R. K., Willingale R., 2017, *Astronomische Nachrichten*, 338, 153
- Brown S., Rudnick L., 2011, *MNRAS*, 412, 2

- Bulbul E., Gaspari M., Alvarez G., Avestruz C., et al. 2019, arXiv e-prints, p. arXiv:1903.04597
- Coccatto L., Arnaboldi M., Gerhard O., Freeman K., Ventimiglia G., Yasuda N., 2010, *A&A*, 519, A95
- Diehl S., Statler T. S., 2006, *MNRAS*, 368, 497
- Donnelly R. H., Markevitch M., Forman W., Jones C., Churazov E., Gilfanov M., 1999, *ApJ*, 513, 690
- Eckert D., Etori S., Pointecouteau E., Molendi S., Paltani S., Tchernin C., 2017, *Astronomische Nachrichten*, 338, 293
- Eckert D., Roncarelli M., Etori S., Molendi S., Vazza F., Gastaldello F., Rossetti M., 2015, *MNRAS*, 447, 2198
- Etori S., Gastaldello F., Leccardi A., Molendi S., Rossetti M., Buote D., Meneghetti M., 2010, *A&A*, 524, A68
- Fabian A. C., Hu E. M., Cowie L. L., Grindlay J., 1981, *ApJ*, 248, 47
- Gaskin J. A., Swartz D. A., Vikhlinin A., Özel F., Gelmis K. E. et al., 2019, *Journal of Astronomical Telescopes, Instruments, and Systems*, 5, 021001
- Gaspari M., Churazov E., 2013, *A&A*, 559, A78
- Ghirardini V., Eckert D., Etori S., Pointecouteau E., Molendi S., Gaspari M., Rossetti M., De Grandi S., Roncarelli M., Bourdin H., Mazzotta P., Rasia E., Vazza F., 2019, *A&A*, 621, A41
- Ghirardini V., Etori S., Eckert D., Molendi S., Gastaldello F., Pointecouteau E., Hurier G., Bourdin H., 2018, *A&A*, 614, A7
- Goodman J., Weare J., 2010, *Appl. Math. Comput. Sci.*, 5, 65
- Grevesse N., Sauval A. J., 1998, *SSR*, 85, 161
- Ichikawa K., Matsushita K., Okabe N., Sato K., Zhang Y.-Y., Finoguenov A., Fujita Y., Fukazawa Y., Kawaharada M., Nakazawa K., et al., 2013, *ApJ*, 766, 90
- Kalberla P. M. W., Burton W. B., Hartmann D., Arnal E. M., Bajaja E., Morras R., Pöppel W. G. L., 2005, *A&A*, 440, 775
- Kawaharada M., Okabe N., Umetsu K., Takizawa M., Matsushita K., Fukazawa Y., Hamana T., Miyazaki S., Nakazawa K., Ohashi T., 2010, *ApJ*, 714, 423
- Kriss G. A., Cioffi D. F., Canizares C. R., 1983, *ApJ*, 272, 439
- Lau E. T., Nagai D., Avestruz C., Nelson K., Vikhlinin A., 2015, *ApJ*, 806, 68
- Lyskova N., Churazov E., Zhang C., Forman W., Jones C., Dolag K., Roediger E., Sheardown A., 2019, *MNRAS*, 485, 2922
- Mahajan S., Singh A., Shobhana D., 2018, *MNRAS*, 478, 4336
- Malavasi N., Aghanim N., Tanimura H., Bonjean V., Douspis M., 2020, *A&A*, 634, A30
- Mushotzky R., Aird J., Barger A. J., Cappelluti N., et al. 2019, arXiv e-prints, p. arXiv:1903.04083
- Nagai D., Kravtsov A. V., Vikhlinin A., 2007, *ApJ*, 668, 1
- Nelson K., Lau E. T., Nagai D., Rudd D. H., Yu L., 2014, *ApJ*, 782, 107
- Neumann D., Arnaud M., Gastaud R., Aghanim N., Lumb D., Briel U., Vestrand W., Stewart G., Molendi S., Mittaz J., 2001, *A&A*, 365, L74
- Neumann D., Lumb D., Pratt G., Briel U., 2003, *A&A*, 400, 811
- Planck Collaboration VIII 2011, *A&A*, 536, A8
- Planck Collaboration X 2013, *A&A*, 554, A140
- Planck Collaboration XIII 2016, *A&A*, 594, A13
- Pratt G. W., Arnaud M., Piffaretti R., Böhringer H., Ponman T. J., Croston J. H., Voit G. M., Borgani S., Bower R. G., 2010, *A&A*, 511, A85
- Roncarelli M., Etori S., Dolag K., Moscardini L., Borgani S., Murante G., 2006, *MNRAS*, 373, 1339
- Sanders J., Fabian A., Churazov E., Schekochihin A., Simionescu A., Walker S., Werner N., 2013, *Sci*, 341, 1365
- Sanders J. S., Fabian A. C., Sun M., Churazov E., Simionescu A., Walker S. A., Werner N., 2014, *MNRAS*, 439, 1182
- Sato T., Matsushita K., Ota N., Sato K., Nakazawa K., Sarazin C. L., 2011, *PASJ*, 63, S991
- Sato T., Sasaki T., Matsushita K., Sakuma E., Sato K., Fujita Y., Okabe N., Fukazawa Y., Ichikawa K., Kawaharada M., Nakazawa K., Ohashi T., Ota N., Takizawa M., Tamura T., 2012, arXiv:1203.1700
- Schuecker P., Finoguenov A., Miniati F., Böhringer H., Briel U., 2004, *A&A*, 426, 387
- Simionescu A., Allen S. W., Mantz A., Werner N., Takei Y., Morris R. G., Fabian A. C., Sanders J. S., Nulsen P. E. J., George M. R., Taylor G. B., 2011, *Science*, 331, 1576
- Simionescu A., Etori S., Werner N., et al. 2019, arXiv e-prints, p. arXiv:1908.01778
- Simionescu A., Werner N., Mantz A., Allen S. W., Urban O., 2017, *MNRAS*, 469, 1476
- Simionescu A., Werner N., Urban O., Allen S., Fabian A., Mantz A., Matsushita K., Nulsen P., Sanders J., Sasaki T., et al., 2013, *ApJ*, 775, 4
- Snowden S. L., Kuntz K. D., 2014, *Cookbook for analysis procedures for XMM-Newton EPIC observations of extended objects and the diffuse background*
- Tchernin C., Eckert D., Etori S., Pointecouteau E., Paltani S., Molendi S., Hurier G., Gastaldello F., Lau E. T., Nagai D., Roncarelli M., Rossetti M., 2016, *A&A*, 595, A42
- Urban O., Simionescu A., Werner N., Allen S. W., Ehlert S., Zhuravleva I., Morris R. G., Fabian A. C., Mantz A., Nulsen P. E. J., Sanders J. S., Takei Y., 2014, *MNRAS*, 437, 3939
- Vazza F., Roncarelli M., Etori S., Dolag K., 2011, *MNRAS*, 413, 2305
- Vikhlinin A., Forman W., Jones C., 1997, *ApJ*, 474, L7
- Voit G. M., Kay S. T., Bryan G. L., 2005, *MNRAS*, 364, 909
- Walker S., Nagai D., Simionescu A., et al. 2019, arXiv e-prints, p. arXiv:1903.04550
- Walker S., Simionescu A., Nagai D., Okabe N., Eckert D., Mroczkowski T., Akamatsu H., Etori S., Ghirardini V., 2019, *Space Science Reviews*, 215, 7
- Walker S. A., Fabian A. C., Sanders J. S., George M. R., 2012, *MNRAS*, 424, 1826
- Walker S. A., Fabian A. C., Sanders J. S., George M. R., Tawara Y., 2012, *MNRAS*, 422, 3503
- Walker S. A., Fabian A. C., Sanders J. S., Simionescu A., Tawara Y., 2013, *MNRAS*, 432, 554
- Watanabe M., Yamashita K., Furuzawa A., Kunieda H., Tawara Y., Honda H., 1999, *ApJ*, 527, 80
- Willson M., 1970, *MNRAS*, 151, 1
- Zhuravleva I., Churazov E., Kravtsov A., Lau E. T., Nagai D., Sunyaev R., 2013, *MNRAS*, 428, 3274
- Zinger E., Dekel A., et al. 2016, *MNRAS*, 461, 412
- Zinger E., Dekel A., et al. 2018, *MNRAS*, 476, 56

APPENDIX A: XMM-NEWTON OBSERVATIONS OF COMA

Table A1 shows the details of all *XMM-Newton* observations used in this work. The outskirts and background pointings are labeled with the words "Outskirts" and "Background", respectively, followed by numerical indices that increase counterclockwise from the Right Ascension (RA) axis. The remaining pointings that cover the central and intermediate regions up to r_{500} are labeled with the word "Inside", followed by numerical indices. In this table,

all outskirts and background observations are new observations, except the observations that labeled "Outskirts10", "Outskirts11", and "Outskirts12". The outskirts pointings that has the same RA and Dec. coordinate set to have the same numerical indices.

APPENDIX B: THERMODYNAMIC PROPERTIES IN AZIMUTHAL SECTORS

In Fig. B1, we show the gas density profiles of the azimuthal sectors obtained from the deprojection of the radial profiles of the X-ray surface brightness using *XMM-Newton* observations. The gas pressure profiles in the azimuthal sectors (Fig. B2), on the other hand, obtained through the SZ effect signal using *Planck* by fitting the projected y profile in each sector to the universal pressure profile (equation 3). From the gas density and pressure profiles, as explained in Section 4, the gas and total masses of the azimuthal sectors were recovered (see Figs B3 and B4). All measurements reported in these figures take account of the systematic uncertainties.

Table A1. *XMM-Newton* observations of Coma

Observation	Obs. ID	Obs. Date	RA (J2000)	Dec. (J2000)	Exposure (ks)
Outskirts1	0841680101	07 Jul 2019	12 55 25.59	+27 47 01.6	23.0
Outskirts2	0841680201	07 Jul 2019	12 55 38.07	+28 17 43.1	23.0
Background1	0841681101	12 Jul 2019	12 53 31.92	+28 29 54.4	29.5
Outskirts3	0841680301	11 Jul 2019	12 57 03.20	+28 41 26.5	26.0
Outskirts4	0841680401	13 Jul 2019	12 59 11.76	+28 52 56.4	23.0
Outskirts5	0841680501	13 Jul 2019	13 01 27.90	+28 51 36.7	23.0
Outskirts6	0841680601	17 Jul 2019	13 03 15.79	+28 32 54.7	23.0
Background2	0841681201	29 Dec 2019	13 05 10.70	+28 53 08.8	23.0
Outskirts7	0841680701	16 Jul 2019	13 04 03.83	+28 04 45.1	26.4
Outskirts8	0841680801	17 Jul 2019	13 03 56.84	+27 35 23.5	34.4
Outskirts9	0841680901	06 Dec 2019	13 02 49.88	+27 11 18.6	30.8
Outskirts10	0800580101	23 Dec 2017	13 00 57.97	+26 58 35.3	80.4
Outskirts10	0800580201	04 Jan 2018	13 00 57.97	+26 58 35.3	87.0
Outskirts11	0403150301	17 Jun 2006	12 57 40.75	+26 56 13.6	56.0
Outskirts11	0403150401	21 Jun 2006	12 57 40.75	+26 56 13.6	64.4
Outskirts12	0058940701	10 Jun 2003	12 55 24.99	+27 13 46.0	22.6
Inside1	0124710501	29 May 2000	12 59 27.49	+27 46 53.0	29.9
Inside2	0124711401	29 May 2000	12 59 46.71	+27 56 60.0	34.6
Inside3	0124711601	11 Jun 2000	12 57 42.51	+27 43 38.0	87.9
Inside4	0124710201	11 Jun 2000	12 57 42.51	+27 43 38.0	41.5
Inside5	0124710901	11 Jun 2000	13 00 32.68	+27 56 59.0	31.2
Inside6	0124710601	12 Jun 2000	12 58 50.01	+27 58 52.0	31.8
Inside7	0124710101	21 Jun 2000	12 56 47.68	+27 24 07.0	41.5
Inside8	0124710401	23 Jun 2000	13 00 04.60	+27 31 24.0	52.8
Inside9	0124711101	24 Jun 2000	12 58 36.51	+28 23 56.0	40.0
Inside10	0124710701	24 Jun 2000	12 57 27.68	+28 08 41.0	27.2
Inside11	0124710301	27 Jun 2000	12 58 32.19	+27 24 12.0	28.6
Inside12	0124712201	09 Dec 2000	12 57 42.51	+27 43 38.0	27.6
Inside13	0124712001	10 Dec 2000	12 58 50.01	+27 58 52.0	22.8
Inside14	0124712101	10 Dec 2000	12 57 27.68	+28 08 41.0	28.1
Inside15	0124710801	10 Dec 2000	13 01 25.60	+27 43 53.0	29.8
Inside16	0153750101	04 Dec 2001	12 59 46.71	+27 56 60.0	25.8
Inside17	0124712401	05 Jun 2002	13 01 50.19	+28 09 28.0	27.6
Inside18	0124712501	07 Jun 2002	13 00 36.50	+28 25 15.0	28.7
Inside19	0204040101	06 Jun 2004	13 00 22.21	+28 24 03.0	101.9
Inside20	0204040201	18 Jun 2004	13 00 22.21	+28 24 03.0	108.3
Inside21	0204040301	12 Jul 2004	13 00 22.21	+28 24 03.0	104.2
Inside22	0300530701	06 Jun 2005	12 59 36.92	+27 58 14.8	25.5
Inside23	0300530601	07 Jun 2005	12 59 35.41	+27 56 33.3	25.7
Inside24	0300530501	08 Jun 2005	12 59 39.73	+27 55 12.0	25.5
Inside25	0300530401	09 Jun 2005	12 59 46.67	+27 55 12.0	27.5
Inside26	0300530301	11 Jun 2005	12 59 51.00	+27 56 33.3	31.0
Inside27	0300530201	17 Jun 2005	12 59 49.45	+27 58 14.8	27.5
Inside28	0300530101	18 Jun 2005	12 59 43.18	+27 58 59.8	25.5
Inside29	0304320301	27 Jun 2005	13 00 22.21	+28 24 03.0	55.9
Inside30	0304320201	28 Jun 2005	13 00 22.21	+28 24 03.0	80.8
Inside31	0304320801	06 Jun 2006	13 00 22.21	+28 24 03.0	63.8
Inside32	0403150201	11 Jun 2006	12 57 42.51	+27 19 09.7	55.2
Inside33	0403150101	14 Jun 2006	12 57 42.51	+27 19 09.7	54.4
Inside34	0652310701	16 Jun 2010	12 57 24.29	+27 29 52.0	21.8
Inside35	0652310201	18 Jun 2010	12 57 24.29	+27 29 52.0	22.3
Inside36	0652310301	20 Jun 2010	12 57 24.29	+27 29 52.0	19.4
Inside37	0652310401	24 Jun 2010	12 57 24.29	+27 29 52.0	23.9
Inside38	0652310501	04 Jul 2010	12 57 24.29	+27 29 52.0	22.9
Inside39	0652310601	06 Jul 2010	12 57 24.29	+27 29 52.0	20.8
Inside40	0652310801	03 Dec 2010	12 57 24.29	+27 29 52.0	16.9
Inside41	0652310901	05 Dec 2010	12 57 24.29	+27 29 52.0	16.9
Inside42	0652311001	11 Dec 2010	12 57 24.29	+27 29 52.0	16.4
Inside43	0691610201	02 Jun 2012	12 57 24.65	+27 29 42.7	37.9
Inside44	0691610301	04 Jun 2012	12 57 24.65	+27 29 42.7	35.9
Inside45	0851180501	30 May 2019	13 02 00.14	+27 46 57.8	48.4

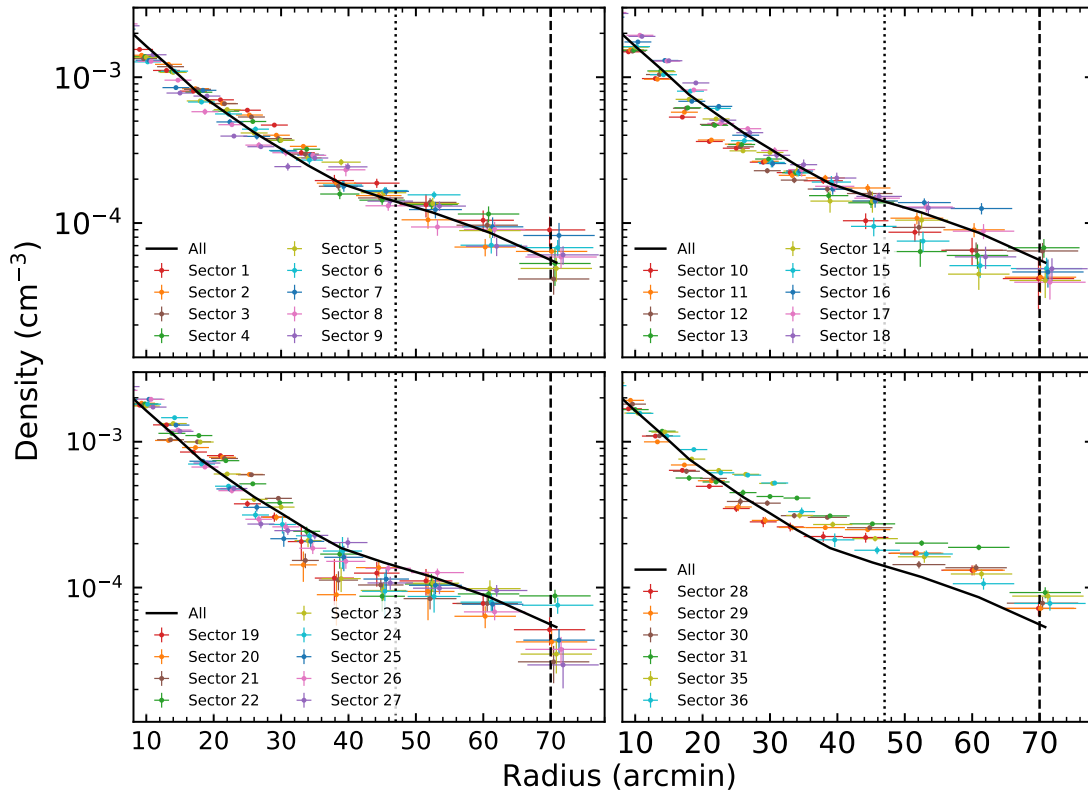


Figure B1. Density profiles in the azimuthal sectors obtained from the deprojection of the surface brightness radial profiles using the onion peeling technique. The error bars are the 1σ percentiles computed using a Monte Carlo technique. The thick black line shows the azimuthally averaged density profile. The vertical dotted and dashed lines represent the r_{500} and r_{200} radii, respectively.

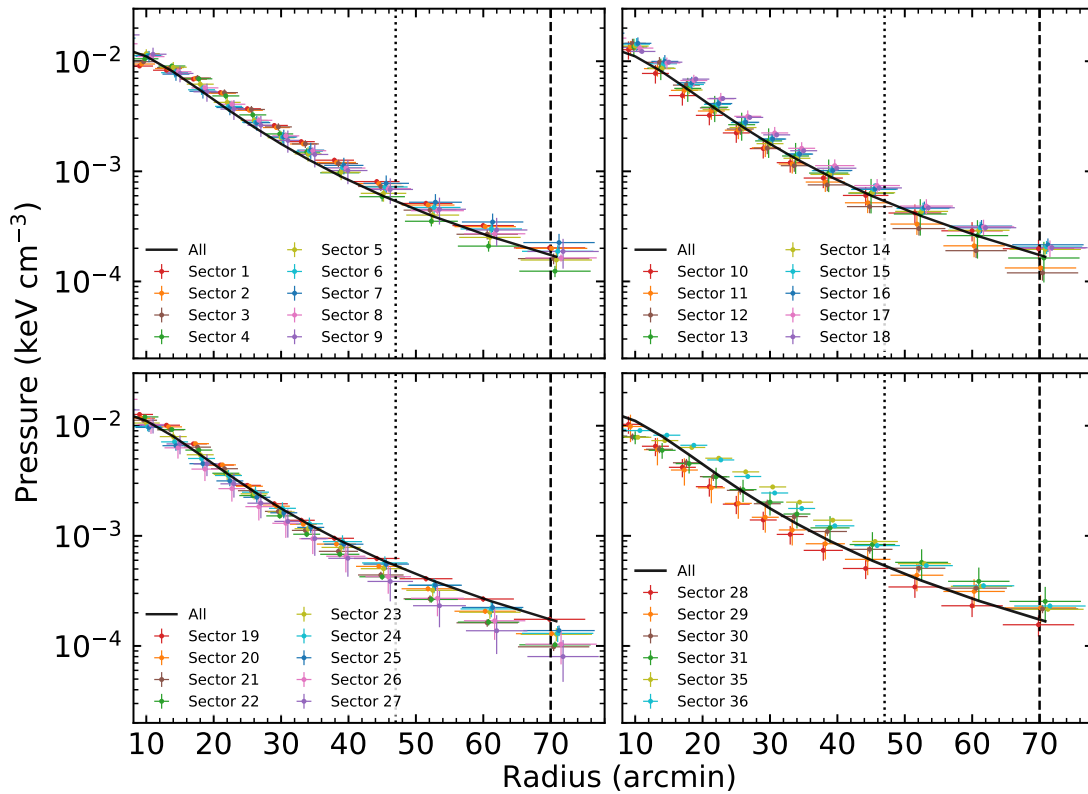


Figure B2. Same as Fig. B1, except for the gas pressure.

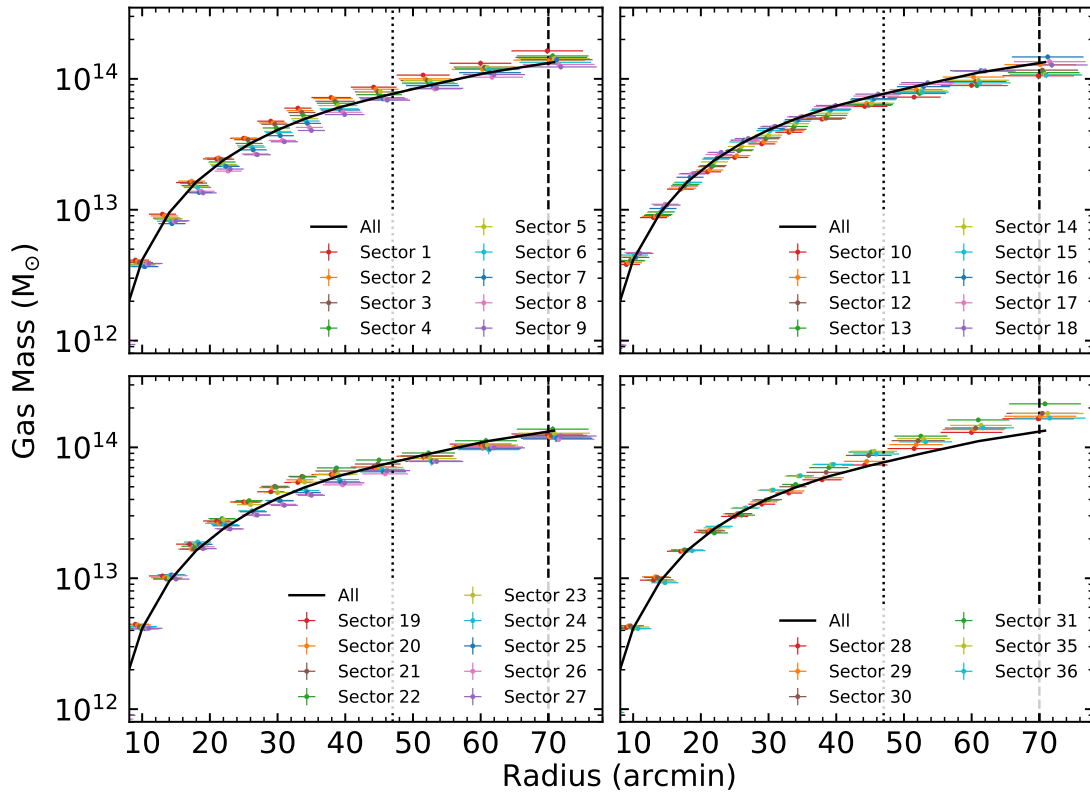


Figure B3. Same as Fig. B1, except for the gas mass.

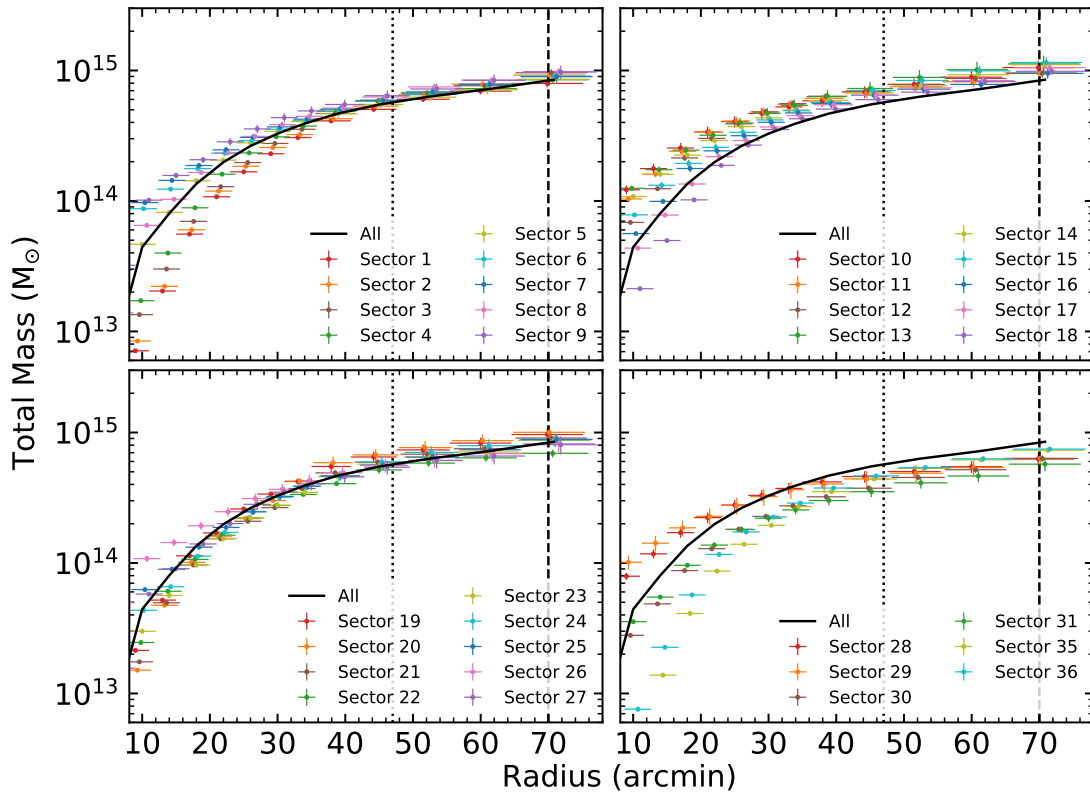


Figure B4. Same as Fig. B1, except for the total mass.